
















## A Disintegrating Rocky World Shrouded in Dust and Gas: Mid-IR Observations of K2-22b using JWST

NICK TUSAY <sup>1,2</sup> JASON T. WRIGHT <sup>1,2</sup> THOMAS G. BEATTY <sup>3</sup> STEVE DESCH <sup>4</sup> KNICOLE COLÓN <sup>5</sup>  
TUSHAR MITTAL <sup>6</sup> HUGH P. OSBORN <sup>7,8</sup> BEATRIZ CAMPOS ESTRADA <sup>9</sup> JAMES E. OWEN <sup>10</sup>  
JESSICA LIBBY-ROBERTS <sup>1,2</sup> ARVIND F. GUPTA <sup>11</sup> BRAD FOLEY <sup>6</sup> ERIK MEIER VALDÉS <sup>12</sup>  
DANIEL J. STEVENS <sup>13</sup> AND ASHLEY HERBST <sup>4</sup>

<sup>1</sup>*Department of Astronomy and Astrophysics, The Pennsylvania State University, University Park, PA, 16802, USA*

<sup>2</sup>*Center for Exoplanets and Habitable Worlds, The Pennsylvania State University, University Park, PA, 16802, USA*

<sup>3</sup>*Department of Astronomy, University of Wisconsin-Madison, Madison, WI, USA*

<sup>4</sup>*School of Earth and Space Exploration, Arizona State University, PO Box 876004, Tempe, 85287-6004, Arizona, USA*

<sup>5</sup>*NASA Goddard Space Flight Center, Greenbelt, MD, 20771, USA*

<sup>6</sup>*Department of Geosciences, The Pennsylvania State University, University Park, PA, 16802, USA*

<sup>7</sup>*NCCR/Planet-S, Physikalisches Institut, Universität Bern, Gesellschaftsstrasse 6, 3012 Bern, Switzerland*

<sup>8</sup>*Inst. f. Teilchen- und Astrophysik, ETH Zürich, Wolfgang-Pauli-Strasse 27, 8093 Zürich, Switzerland*

<sup>9</sup>*Max-Planck-Institut für Astronomie, Königstuhl 17, D-69117 Heidelberg, Germany*

<sup>10</sup>*Astrophysics Group, Imperial College London, Blackett Laboratory, Prince Consort Road, London SW7 2AZ, UK*

<sup>11</sup>*U.S. National Science Foundation National Optical-Infrared Astronomy Research Laboratory, 950 N. Cherry Ave., Tucson, AZ 85719, USA*

<sup>12</sup>*University of Oxford, Oxford, UK*

<sup>13</sup>*Department of Physics and Astronomy, University of Minnesota Duluth, Duluth, Minnesota 55812, USA*

### ABSTRACT

The disintegrating ultra-short period rocky exoplanet K2-22b periodically emits dusty clouds in a dynamically chaotic process resulting in a variable transit depth from 0–1.3%. The effluents that sublimate off the surface and condense out in space are probably representative of the formerly interior layers convectively transported to the molten surface. Transmission spectroscopy of these transiting clouds reveal spectral fingerprints of the interior composition of this rocky world. We used JWST’s Mid-Infrared Instrument (MIRI) as a low-resolution slitless spectrograph to observe four predicted transit windows for K2-22b. For each observation, we extracted a transmission spectrum over the spectral range of 4.3–11.8  $\mu\text{m}$ . We detect one transit at high significance and two at low significance. We find that the data 1) disfavor featureless, iron-dominated core material, 2) are consistent with some form of magnesium silicate minerals, likely from mantle material, and 3) show a distinct and unexpected feature at  $\sim 5 \mu\text{m}$ . The unexpected feature, also seen weakly in the low-significance transits, is consistent with some gas features, possibly NO and/or CO<sub>2</sub>. These findings warrant further study to improve the constraints on the composition of this disintegrating rocky world.

### 1. INTRODUCTION

Protoplanetary disks (e.g. Thiabaud et al. 2015), debris disks (e.g. Hughes et al. 2018), and polluted White Dwarfs (WDs) (e.g. Jura & Young 2014; Vanderburg et al. 2015) provide glimpses into the constituents of planetary bodies from the beginning and end stages of a system’s life-cycle. Studies on such systems have also been used to assess the relationships between host star metallicity and the material available in their planets (Wang et al. 2019; Adibekyan et al. 2021; Swain et al. 2024, e.g.). However, these approaches, while valuable, are only indirect probes of the compositions of planets. Various planetary accretion and geophysical processes can significantly impact the composition and evolution of planets over their star’s main sequence phase (Ballmer & Noack 2021; Foley 2024).

Corresponding author: Nick Tusay

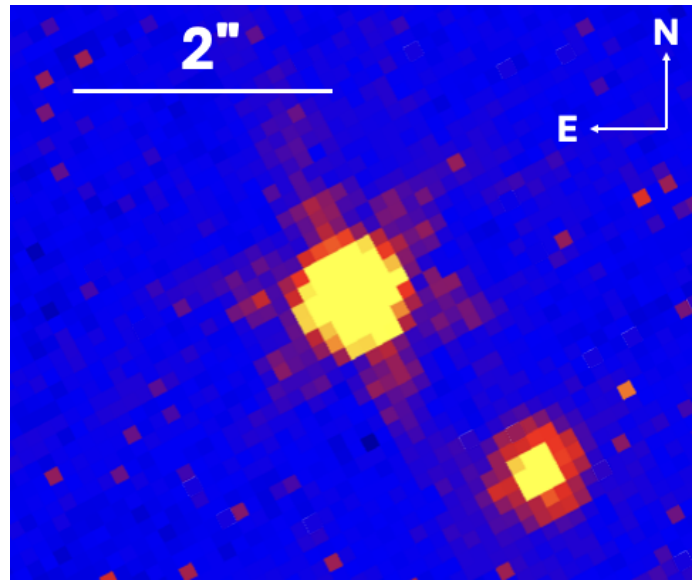
tusay@psu.edu

The interior composition of terrestrial planets and its coupling with the surface-atmosphere is of particular interest to the astrobiological community for assessing planetary habitability. Measurements on planet bulk density have severe compositional degeneracies, especially with regard to a planet’s interior versus surface volatile reservoirs—these are strongly influenced by geophysical processes and, in turn, impact continued planetary habitability (Seager et al. 2007; Dorn et al. 2015; Cockell et al. 2024). With only the planets in our Solar System for comparison, and no clear understanding of how unique our system is, we need more data on other systems to tease out details on interior and geophysical processes for extrasolar planets. But fully formed planets in stable orbits around main sequence stars have a habit of keeping their rocky interiors on the inside, making the truth of their constituents difficult to access. Disintegrating exoplanets offer a unique opportunity to directly probe the interior composition of rocky exoplanets (Bodman et al. 2018). As a unique sub-class of ultra-short period planets (USPs,  $\lesssim 24$ hr orbits), disintegrating planets are not close enough to their host star to be gravitationally disrupted but hot enough that their interior layers likely convect with a molten surface that ultimately sublimates out into space (Rappaport et al. 2012).

K2-22b is one of only three rocky USPs detected by the *Kepler* and *K2* missions that are theorized to be actively disintegrating due to their proximity to its host star. K2-22b transits a relatively bright, early M-dwarf ( $K = 11.91$ ,  $T_{\text{eff}} = 3830$  K) with an orbital period of 9.1457 hours (Sanchis-Ojeda et al. 2015). The dramatic variability in lightcurve transit depth (0–1.3%) combined with the asymmetric transit shape suggests we are observing a transient cloud of dust sublimating off the surface of an otherwise unseen planet (Rappaport et al. 2012). Simulations of the chaotic outflows from this class of planet have been used to show that the dynamic evolution of the transiting dust cloud model is plausible over orbital timescales (Bromley & Chiang 2023). Hydrodynamical models of dust outflow geometry suggest K2-22b is a less massive planet than the similar object Kepler-1520b (KIC 12557548b; hereafter “KIC 1255b”), and particles escape the surface in a manner between the extremes of purely day-side and spherical outflow (Campos Estrada et al. 2024). There is likely a complex interplay between the optical depth of the resulting cloud and the particles that can further condense out and add to it (Bromley & Chiang 2023). Clouds of significantly differing optical depth may thus exhibit variations in abundance measurements of certain compositional elements.

Having likely persisted in this state of constantly vaporizing surface material, the deeper layers of the planet may at this point be convecting to the surface or completely exposed through significant mass loss (Perez-Becker 2013; Curry et al. 2024a). Thus, measuring the composition of these dusty effluents can probe the bulk composition of what used to be the interior of the planet, as it is vaporized (Curry et al. 2024b). Previous studies of KIC 1255b and KOI-2700b (the two other known disintegrating USP planets) have shown through dynamical-modeling constraints that the dust in their tails might be composed of corundum ( $\text{Al}_2\text{O}_3$  [s]) or iron-rich silicates, while other compositions such as pure iron or graphite have been ruled out (van Lieshout et al. 2014, 2016). More recently, modeling efforts by Bromley & Chiang (2023) and Campos Estrada et al. (2024) have found iron-bearing silicates to be the most likely composition of the dust for K2-22b and KIC 1255b.

K2-22b’s variable behavior has persisted well beyond the *K2* mission (Colón et al. 2018; Schlawin et al. 2021), though recent observations indicate a long-term trend of quiescence (Gaidos et al. 2024). However, this is not entirely unprecedented, as the disintegrating planet KIC 1255b has been observed with a similar reduction in activity (Schlawin



Transit #	Time & Date (UTC)	Transit Depth (ppm)
1	18:01:42 April 24, 2024	$290 \pm 396$
2	15:45:27 April 26, 2024	$230 \pm 315$
3	10:02:57 April 27, 2024	$170 \pm 291$
4	4:20:27 April 28, 2024	$1600 \pm 177$

**Table 1.** JWST Cycle 2 GO Program 3315 observations.

*Top image:* MIRI verification image of K2-22 and its smaller companion star, at  $\sim 2''$  separation.

*Bottom table:* Expected mid-transit times and dates, calculated from the ephemeris of Schlawin et al. (2021), and transit depth measurements during these JWST observations of K2-22b.

et al. 2016), only to return to its original activity levels a few years later (Schlawin et al. 2018). Several plausible interpretations for the long-term variability have been suggested: planet-star magnetic field interactions, variations in stellar activity (Kawahara et al. 2013), or substellar magma pool compositional variations (Kite et al. 2016). Long-term monitoring is required to provide observational constraints on the underlying mechanisms for this time evolution (Gaidos et al. 2024).

In this paper, we present the results of the first infrared spectroscopic measurements of K2-22b. These measurements were made using the Mid-Infrared Instrument (MIRI) in low-resolution spectroscopy (LRS) mode on JWST. In Section 2, we describe the JWST observations, simultaneous optical observations with the CHaracterising ExOPlanet Satellite (CHEOPS), and the subsequent data analysis methods used to obtain the spectra. In Section 3, we discuss the mineralogy models we used for comparison and present the results of our analysis. In Section 4, we provide a detailed interpretation of the results and the impact they have on planetary interiors. Additional plots are included in the appendix.

## 2. OBSERVATIONS AND ANALYSIS

### 2.1. Infrared Observations with JWST

Through GO Program 3315 (PI: Wright, Science PI: Tusay), we used the MIRI LRS instrument on JWST to observe (a) 2 individual transits of K2-22b, and (b) a full phase curve including 2 additional transits, using the latest ephemeris from Schlawin et al. (2021). Table 1 provides a summary list of the observations.

The roll angle of the telescope was such that the dispersion of the light was not contaminated by the companion star, spatially separated by about  $2''$ . The spatial separation is sufficiently wide to create an aperture around the target star that can collect a majority of its light without contamination by the companion. More details on the apertures used in §2.3 and §2.4. The response of the slitless spectrograph yielded measurements from 4.3 to 11.8  $\mu\text{m}$ .

### 2.2. Optical Observations with CHEOPS

CHEOPS is a 30-cm aperture space telescope that observes transiting exoplanets at optical wavelengths, with a bandpass from 330 to 1100 nm (Benz et al. 2021). It is located in a nadir-locked low-Earth orbit, meaning that the field rotates once every  $\sim 100$  minutes, with typically  $\sim 40$  minutes affected by Earth occultation.

We obtained three separate CHEOPS observations in a 3-day window via a Director’s Discretionary Time (DDT) proposal (DDT-0020) in order to constrain the optical depth of K2-22b. These observations were taken to be simultaneous with the observations from JWST. We targeted the same individual transit times and full phase curve. For the individual transits, assuming a 0.8hr transit window, we allowed for 4.1 hours of baseline before and after each transit. Similarly, we obtained a baseline of 4.1 hours before and after the transits for the full phase curve.

To extract precise photometry and remove systematics (e.g. due to field rotation) we used PSF photometric extraction using the PIPE package (see e.g. Fortier et al. 2024)<sup>1</sup>. We then performed a combined model using `cheoplanet` (see e.g. Egger et al. 2024)<sup>2</sup> which models a spline with 9-degree flux spacing against roll angle, as well as linear & quadratic parameter decorrelation (e.g., with various incidental time series including centroid, background, onboard temperature, etc.).

However, many of the K2-22b transits in our observing windows were impacted by earth occultation gaps. Only the 4th transit window, and fortuitously the most significant transit event, lined up with an unobstructed observing window for CHEOPS. Figure B4 shows the CHEOPS lightcurve for this 4th transit window, fit with the same transit model as described in §2.5. The magnitude of K2-22b ( $G = 14.93$ ) is technically beyond the rated ( $G = 6 - 12$ ) magnitude limit of CHEOPS (Fortier et al. 2024). The result was a photometric lightcurve with an RMS of 2371 ppm per 30-min bin.

### 2.3. Data Reduction with Eureka!

We reduced the Stage 0 uncal JWST data products from MAST using the `Eureka!`<sup>3</sup> pipeline with the standard configuration files for the MIRI instrument (Bell et al. 2022). We tested a range of apertures to account for background contamination from the companion star. Using the apertures that produced the minimum noise profiles, we ran Stage 1 to Stage 4 to obtain time series flux measurements over each observed exposure in 300 spectral channels from 4.3 to

<sup>1</sup> <https://github.com/alphapsa/PIPE>

<sup>2</sup> <https://github.com/hposborn/chexoplanet>

<sup>3</sup> <https://github.com/kevin218/Eureka!>

11.8  $\mu\text{m}$ . The same data reduction process was used for all 4 observations, with the only difference being the optimal apertures selected for each observation. We used vertical axis rows 150 to 393 along the dispersion axis, and horizontal axis columns 10 to 67. For transits 1 & 2, we selected 15 pixels for the half-width aperture around K2-22 and 25 pixels as the start of the background aperture to effectively mask out the companion. For transits 3 & 4, we used half-width apertures of 6 and 19 for the target and background, respectively.

#### 2.4. Pegasus Data Reduction

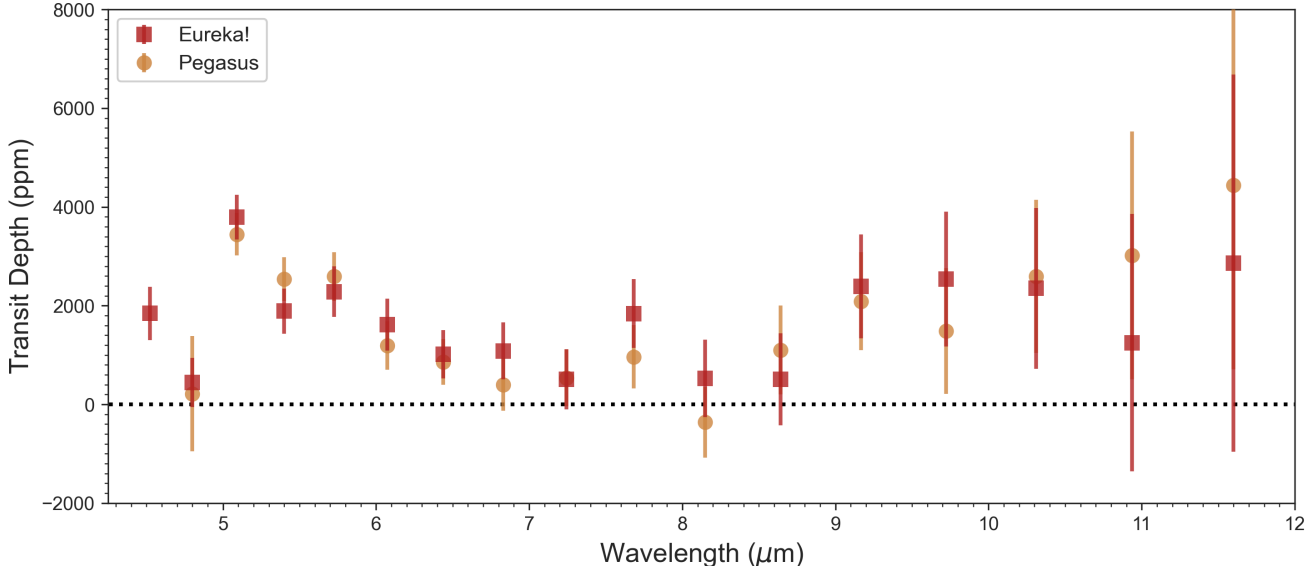


**Figure 1.** Two independent reductions of the MIRI LRS data for transit 4 agree within their uncertainties. Shown are our fiducial *Eureka!* results (Section 2.3) and the results from a reduction using the *Pegasus* pipeline (Section 2.4), plotted with their associated  $1\sigma$  uncertainties at a constant spectral resolution of  $R = 17$ . Both reductions agree on the overall shape of the transmission spectrum and are consistent with each other to within  $1\sigma$ .

As an independent check on the *Eureka!* data reduction described in Section 2.3, we also reduced the observations using the *Pegasus* pipeline<sup>4</sup>, which has been used for NIRC*am* (Beatty et al. 2024; Welbanks et al. 2024; Schlawin et al. 2024a) and NIRS*pec* (Schlawin et al. 2024b) transit and eclipse observations. Our reduction began with background subtraction on the RATEINTS files provided by version 1.13.3 of the *jwst* pipeline using CRDS version 11.17.14. We first performed a general background subtraction step for each RATEINTS file by fitting a two-dimensional, second-order spline to each integration using the entire  $72 \times 416$  RATEINTS images. For the background fitting, we masked columns 0 to 12 and 67 to 723 to remove the non-imaged sections of the subarray. To prevent self-subtraction, we also masked out starlight from K2-22 by masking pixels in columns 29 to 45 and above row 50, and from the companion star by masking the pixels in columns 15 to 25 and above row 150. We then performed a single round of  $3\sigma$  clipping on the unmasked portions of the image. We then fit a spline to the unmasked, unclipped pixel values with a median-box size of 5 pixels. We extrapolated the combined background spline for the whole image over the masked portions near K2-22 and the companion star and subtracted it from the original image values. We then removed the alternating row and column horizontal and vertical banding in the background-subtracted images by calculating the biweight mean of each row or column, and then subtracting this mean from each row or column. In both cases, we used the same starlight-mask as for the spline fitting to avoid self-subtraction.

We then extracted broadband and spectroscopic lightcurves from our background-subtracted images. To do so, we fit the spectral trace using a fourth-order polynomial and then used optimal extraction to measure the 1D spectrum in each image. We performed three rounds of iterative profile estimation for the optimal extraction routine, after which we judged the profile fit to have converged. Using the resultant 1D spectra, we extracted a broadband lightcurve from 4.65  $\mu\text{m}$  to 11.95  $\mu\text{m}$ . For the spectroscopic lightcurves, we subdivided this wavelength region into 17 spectral channels

<sup>4</sup> <https://github.com/TGBeatty/PegasusProject>

spaced at a constant spectral resolution of  $R = 17$ . For both the broadband and spectroscopic lightcurves, we linearly interpolated over each spectral column to account for partial-pixel effects in the wavelength solutions.

Figure 1 shows that independent reduction pipelines produce good agreement of the observed transit spectrum.

### 2.5. Data Analysis

The target of these observations is an ephemeral cloud of dust and gas, rapidly evolving over the timescale of a single orbit ( $\sim 9$  h), and the shape and depth of an individual transit deviates unpredictably from the classic solid-body transit model. Due to the unique nature of this object, subsequent analysis of the data was done using bespoke python code to normalize and model the lightcurve transit. The time series output from *Eureka!* was curated by removing the first 30 minutes of data to account for instrument settling (Bell et al. 2023; Bouwman et al. 2023; Matsuo et al. 2019), and then removing  $> 3\sigma$  outliers from the stellar spectrum (see Figure A1).

Using the cleaned data, we first plotted the white lightcurve for each observation and identified a clear transit during the fourth expected transit window. Focusing first on the most significant detection, we modeled the transit in white light, and then applied this model to each channel in order to measure the spectroscopic depth. The primary model chosen is a simple 2-degree polynomial over the transit window that goes to zero at the window edges. The average lightcurve from the original *K2* data and a simple boxcar were also tested as models, resulting in no significant difference in the derived spectrum, verifying that our results are not sensitive to this choice.

The model depth,  $\delta$ , was calculated from

$$\delta = \frac{\sum_i y_i f_i / \sigma_i^2}{\sum_i f_i^2 / \sigma_i^2}, \quad (1)$$

where  $y$  is the measured normalized flux,  $f$  is the model, and  $\sigma$  is the uncertainty in each data point, as measured by the standard deviation of the baseline flux. Due to the unknown extent of the transiting cloud, the baseline flux was conservatively chosen outside  $1.5\times$  the 46 minute transit duration window calculated by Sanchis-Ojeda et al. (2015) and centered at the ephemeris from Schlawin et al. (2021). The model depth variance,  $\sigma_\delta^2$ , is calculated as

$$\sigma_\delta^2 = \frac{1}{\sum_i f_i^2 / \sigma_i^2}. \quad (2)$$

We then applied these same techniques to the lightcurves and spectra of the other observations.

## 3. MINERALOGY COMPARISON AND RESULTS

### 3.1. Solid Mineralogy

We use Mie theory (Mie 1908) to compute the opacity of common dust species expected to be abundant in different layers of an Earth-like rocky planet. We pick Earth-like species following previous modeling results which find them to be the most likely (Bromley & Chiang 2023; Campos Estrada et al. 2024). We assume the dust grain sizes to be power-law distributed between 0.01 and  $5 \mu\text{m}$ , with an effective size of  $1 \mu\text{m}$  and an index of 0.875. The choice of dust grain sizes is based on morphological modeling of these objects by Sanchis-Ojeda et al. (2015), van Lieshout et al. (2016) and Schlawin et al. (2021).

We considered Fe [s], FeO [s], and FeS [s] as likely planetary core constituents. For the mantle, we considered enstatite ( $\text{MgSiO}_3$  [s]), forsterite ( $\text{Mg}_2\text{SiO}_4$  [s]), fayalite ( $\text{Fe}_2\text{SiO}_4$  [s]), olivine ( $(\text{MgFe})_2\text{SiO}_4$  [s]), and quartz ( $\text{SiO}_2$  [s]). We also considered corundum ( $\text{Al}_2\text{O}_3$  [s]) as it was found to be the most likely dust species in the similar object KIC 1255b by van Lieshout et al. (2016). The references for the dust optical data used are presented in Table E1. Additionally, we used the reflectance/emissivity data from a large natural mineralogy library—JPL ECOSTRESS spectral library (Meerdink et al. 2019). Figure D6 compares the spectrum of the fourth transit with the opacities for the solid dust species we considered. The key focus of this analysis is to assess (a) if we are observing the planetary core or the mantle/crust, and (b) if there are any minerals with strong emissions in the  $4.3\text{--}6 \mu\text{m}$  range, especially around  $5 \mu\text{m}$ .

The long-wavelength features may be consistent with some combination of solid mantle/crust mineralogy, but the significant transparency and opacity features seen at  $4.3\text{--}6 \mu\text{m}$  cannot be explained by any combination of the solid dust species we considered.

### 3.2. Gas Mineralogy

The spectrum of the fourth transit, seen in Figure D6, shows a striking feature around  $5 \mu\text{m}$ , where all solid models we considered exhibit smoothly continuous moderate opacity. This potentially suggests the presence of a gas species.

We searched the DACE database (Grimm et al. 2021) for comparable gas features and tested sets of species that are expected for a vaporizing Earth-like rocky planet (e.g. Schaefer & Fegley 2009; Miguel et al. 2011): CaO, TiO, AlO, MgO, SiO. The resulting opacities for the two most plausible of these species, MgO and SiO can be seen in Figure D7. Since none of the expected rock vapor species were found to be good matches to the data, we also considered species known to be present in icy bodies in the solar system: CO, CO<sub>2</sub>, NO, N<sub>2</sub>, H<sub>2</sub>O. The resulting opacities for the two most convincing of these species, NO and CO<sub>2</sub> can be seen in Figure D8. Finally, we considered more exotic rock-vapor species: FeH, SiS, SiN. None of the resulting opacities for these less plausible species matched the data. The optical opacity from the CHEOPS photometry measurements, despite large uncertainty, disfavors gas species with extreme optical opacity, such as Fe and MgO (see Figure D7).

### 3.3. Results

We report a single detection of significance measured at  $1600 \pm 177$  ppm during the 4th expected transit window. No significant transits were detected at the other transit windows (see Table 1). The distribution of transit depths from K2 suggested 4 transits offered a 95% chance at observing at least a 0.5% cumulative depth. Other recent observations using ground-based multi-band optical photometry to monitor this object indicate that K2-22b is experiencing a long-term quiescent trend (Gaidos et al. 2024).

Figure 2 shows the white light time series of the second half of the phase curve, including the only significant transit event detected by JWST and the resulting transmission spectrum. A flat spectrum is strongly disfavored ( $\Delta\chi^2_v = 2.98$ ). The transit is most significantly detected at  $5.1\mu\text{m}$ , consistent with nitric oxide (NO) gas, in contrast to a clear non-detection at  $4.8\mu\text{m}$ . After analyzing a large suite of minerals, we do not find a suitable mineral with solid-state features consistent with the  $4.8\text{--}5.1\mu\text{m}$  feature (and the spectra at other wavelengths). Features in the data at longer wavelengths are consistent with some combination of expected iron-magnesium-silicate species (Bodman et al. 2018; Campos Estrada et al. 2024), but the large uncertainties from the single spectrum cannot distinguish between them.

We also detect transits at low significance in the other three transit windows (see Figures B2 & C5). Intriguingly, in two out of these three transit windows the most significant detections are in the  $4.5$  and  $5.1\mu\text{m}$  channels, which provides an additional line of evidence that these features in transit window 4 are real absorption features and not a statistical fluke or result of systematic uncertainties.

## 4. DISCUSSION

Assessing the habitability of rocky exoplanets requires knowledge of their interior compositions and mineralogy, which otherwise cannot be directly observed (although it can be inferred for some planets in the Solar System). Although USPs are undoubtedly inhospitable, they provide a unique case study for determining the compositions for a whole family of similar terrestrial planets and ascertaining deviations (or lack thereof) from their host-star compositions. Observations of USPs like K2-22b provide the opportunity to compare to observed stellar elemental abundances to constrain the interior compositions of more temperate extant rocky exoplanets.

Terrestrial rocky planets generally differentiate into metal-rich cores, rocky mantles, and chemically distinct crusts. Earth’s mantle is silicate-rich (mostly MgSiO<sub>3</sub> with some small Fe/Mg ratio) (e.g. Kargel & Lewis 1993; O’Neill & Palme 1998). Thus, the most likely minerals to condense from a cloud of mantle vapor would be expected to be enstatite (MgSiO<sub>3</sub>) and forsterite (Mg<sub>2</sub>SiO<sub>4</sub>). However, recent modeling by Campos Estrada et al. (2024) suggests a composition of magnesium–iron olivines or pyroxenes best explains the average transit shape of K2-22b. Similarly, Bromley & Chiang (2023) argued that iron-bearing silicates are required to be able to produce an observable mass loss rate for catastrophically evaporating exoplanets. Figure 2 demonstrates that improved long-wavelength ( $\gtrsim 8\mu\text{m}$ ) spectral fidelity is critical to testing these hypotheses. However, the features seen at these longer wavelengths are at least consistent with rocky silicate, as opposed to an iron core composition.

Additionally, Booth et al. (2023) hinted at opacity from likely gas species outgassing during the vaporization process. The shorter MIRI wavelength features in the top panel spectrum in Figure 2 may constitute the first direct observations of gas features from an evaporating planet. Unexpectedly, the models that best fit these measurements seem to be ice-derived species (NO and CO<sub>2</sub>). This is counter-intuitive to what we might expect from the evaporation of a rocky mantle and demands follow-up JWST observations for verification. One potential scenario to form these species could be photo-dissociation (X-ray and EUV) and collisional dissociation (via energetic electrons) of molecular nitrogen and water vapor (from water ice) (Marsh et al. 2004; Sinnhuber et al. 2012; Bulak et al. 2022). Alternatively, the NO can be produced by sublimation of H<sub>2</sub>O and NH<sub>3</sub> ices followed by gas phase chemistry through OH and NH, a mechanism

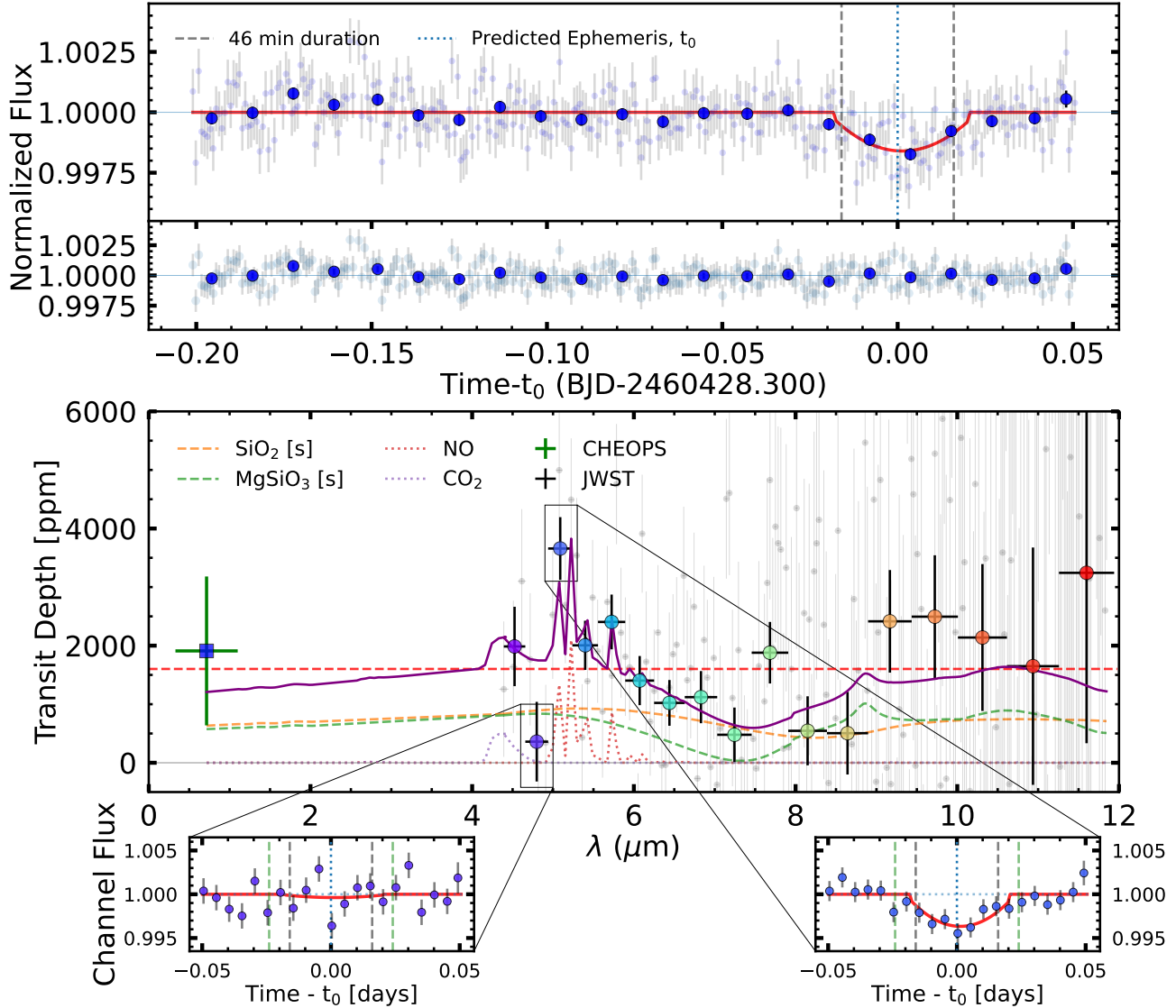


**Figure 2.** Results from JWST Cycle 2 GO Program 3315.

**Top:** Lightcurve of the second half of the phase curve, collected on April 28, 2024, showing a clear transit at the predicted ephemeris. The unbinned time series data is plotted in grey in the background. The blue points are binned to a time resolution of 8 minutes. The average 46-minute duration drawn from Sanchis-Ojeda et al. (2015) is shown as vertical dashed grey lines for reference. Since the transit duration incorporating the cloud of material is not precisely known and potentially variable with wavelength, the baseline flux was calculated from data outside the baseline boundaries set at  $1.5\times$  the average 46-minute duration, centered at the ephemeris and shown as vertical dashed green lines. The red line is a 2nd order polynomial model fit to the data during transit and set to zero elsewhere. The residuals of the lightcurve model are shown in the bottom panel.

**Middle:** JWST MIRI spectrum showing a clear detection of a transit from  $4.3\text{--}7\ \mu\text{m}$  except at  $4.8\ \mu\text{m}$ . The unbinned JWST data for each channel is plotted in grey in the background. The binned JWST spectrum in the foreground has a constant spectral resolution of  $R=17$ . The horizontal red dashed line shows the overall transit depth from the MIRI lightcurve in the top panel. The dotted curves show the spectra models of plausible gas species from the DACE database (Grimm et al. 2021). The dashed curves show representative combinations of iron-magnesium-silicate species predicted by Bodman et al. (2018); Campos Estrada et al. (2024). The solid purple line shows a total opacity model representing a combination of these minerals and gases with features that plausibly correspond to features in the data. CHEOPS photometry is also shown over its  $0.33\text{--}1.1\ \mu\text{m}$  bandpass. The measured CHEOPS transit depth is consistent with the overall transit depth from the MIRI lightcurve.

**Bottom Insets:** The lightcurve and transit models in two channels that illustrate an unexpected spectrum feature with the most significance at  $\sim 5\ \mu\text{m}$ . A flat spectrum is disfavored ( $\Delta\chi^2_\nu = 2.98$ , or  $3.7\sigma$ ). The unexpected feature at  $5.1\ \mu\text{m}$ , consistent with nitric oxide (NO) gas is clearly detected, in contrast to a clear non-detection at  $4.8\ \mu\text{m}$  (see Figure D8).

that has been partially used to explain NO observations in some proto-stellar objects (Kulterer et al. 2024). A potential geophysical situation wherein we might get the right combination of gas and dust species (as inferred from our JWST data analysis) is the evaporation of a mantle layer with some mixture of  $\text{N}_2$ - $\text{NH}_3$ - $\text{CO}_2$  ice clathrates (at the base of a deep icy ocean world) (Journaux et al. 2020; Carnahan et al. 2022) and/or magmatic degassing of  $\text{N}_2$ ,  $\text{CO}_2$ , and  $\text{H}_2\text{O}$  dissolved in the magma ocean (Chazallon & Pirim 2018; Scarpa et al. 1996). However, confirming the spectral features seen for K2-22b with additional data from JWST is critical to better assess the plausible geophysical scenarios in detail with theoretical models and compare gas abundances with thermo-chemical models with sublimation and gas-particle chemistry.

The results of these observations offer strong support for the disintegrating planet model for K2-22b and validate this technique to explore the chemical composition of exoplanetary interiors. It also demonstrates the promise of using JWST to further explore this and other similar targets, such as KIC 1255b and the newly discovered BD+05 4868 Ab (Hon et al. 2025).

#### ACKNOWLEDGEMENTS

This work is based on observations made with the NASA/ESA/CSA James Webb Space Telescope. The data were obtained from MAST at STScI, which is operated by the Association of Universities for Research in Astronomy, Inc., under NASA contract NAS 5-03127 for JWST. These observations are associated with GO Program 3315.

Support for GO Program 3315 was provided by NASA through a grant from the Space Telescope Science Institute, which is operated by the Association of Universities for Research in Astronomy, Inc., under NASA contract NAS 5-03127.

This material is based upon work supported by the National Science Foundation Graduate Research Fellowship Program under Grant No. DGE1255832.

The work of HPO has been carried out within the framework of the NCCR PlanetS supported by the Swiss National Science Foundation under grants 51NF40\_182901 and 51NF40\_205606.

The Center for Exoplanets and Habitable Worlds and the Penn State Extraterrestrial Intelligence Center are supported by Penn State and its Eberly College of Science.

*Facilities:* JWST (MIRI LRS), CHEOPS

*Software:* Astropy (Astropy Collaboration et al. 2013, 2018, 2022), Eureka! (Bell et al. 2022), Pegasus

#### REFERENCES

- Adibekyan, V., Dorn, C., Sousa, S. G., et al. 2021, *Science*, 374, 330, doi: [10.1126/science.abg8794](https://doi.org/10.1126/science.abg8794)
- Astropy Collaboration, Robitaille, T. P., Tollerud, E. J., et al. 2013, *A&A*, 558, A33, doi: [10.1051/0004-6361/201322068](https://doi.org/10.1051/0004-6361/201322068)
- Astropy Collaboration, Price-Whelan, A. M., Sipőcz, B. M., et al. 2018, *AJ*, 156, 123, doi: [10.3847/1538-3881/aabc4f](https://doi.org/10.3847/1538-3881/aabc4f)
- Astropy Collaboration, Price-Whelan, A. M., Lim, P. L., et al. 2022, *ApJ*, 935, 167, doi: [10.3847/1538-4357/ac7c74](https://doi.org/10.3847/1538-4357/ac7c74)
- Ballmer, M. D., & Noack, L. 2021, *Elements*, 17, 245, doi: [10.2138/gselements.17.4.245](https://doi.org/10.2138/gselements.17.4.245)
- Beatty, T. G., Welbanks, L., Schlawin, E., et al. 2024, *ApJL*, 970, L10, doi: [10.3847/2041-8213/ad55e9](https://doi.org/10.3847/2041-8213/ad55e9)
- Begemann, B., Dorschner, J., Henning, T., et al. 1997, *ApJ*, 476, 199, doi: [10.1086/303597](https://doi.org/10.1086/303597)
- Bell, T. J., Ahrer, E.-M., Brande, J., et al. 2022, *Journal of Open Source Software*, 7, 4503, doi: [10.21105/joss.04503](https://doi.org/10.21105/joss.04503)
- Bell, T. J., Kreidberg, L., Kendrew, S., et al. 2023, arXiv e-prints, arXiv:2301.06350, doi: [10.48550/arXiv.2301.06350](https://doi.org/10.48550/arXiv.2301.06350)
- Benz, W., Broeg, C., Fortier, A., et al. 2021, *Experimental Astronomy*, 51, 109
- Bodman, E. H., Wright, J. T., Desch, S. J., & Lisse, C. M. 2018, *The Astronomical Journal*, 156, 173
- Booth, R. A., Owen, J. E., & Schulik, M. 2023, *MNRAS*, 518, 1761, doi: [10.1093/mnras/stac3121](https://doi.org/10.1093/mnras/stac3121)
- Bouwman, J., Kendrew, S., Greene, T. P., et al. 2023, *PASP*, 135, 038002, doi: [10.1088/1538-3873/acbc49](https://doi.org/10.1088/1538-3873/acbc49)
- Bromley, J., & Chiang, E. 2023, *MNRAS*, 521, 5746, doi: [10.1093/mnras/stad932](https://doi.org/10.1093/mnras/stad932)
- Bulak, M., Paardekooper, D., Fedoseev, G., et al. 2022, *Astronomy & Astrophysics*, 657, A120
- Campos Estrada, B., Owen, J. E., Jankovic, M. R., Wilson, A., & Helling, C. 2024, *MNRAS*, 528, 1249, doi: [10.1093/mnras/stae095](https://doi.org/10.1093/mnras/stae095)
- Carnahan, E., Vance, S. D., Hesse, M. A., Journaux, B., & Sotin, C. 2022, *Geophys. Res. Lett.*, 49, e97602, doi: [10.1029/2021GL097602](https://doi.org/10.1029/2021GL097602)



- Chazallon, B., & Pirim, C. 2018, *Chemical Engineering Journal*, 342, 171
- Cockell, C. S., Simons, M., Castillo-Rogez, J., et al. 2024, *Nature Astronomy*, 8, 675, doi: [10.1038/s41550-024-02196-w](https://doi.org/10.1038/s41550-024-02196-w)
- Colón, K. D., Zhou, G., Shporer, A., et al. 2018, *The Astronomical Journal*, 156, 227
- Curry, A., Booth, R., Owen, J. E., & Mohanty, S. 2024a, *MNRAS*, 528, 4314, doi: [10.1093/mnras/stae191](https://doi.org/10.1093/mnras/stae191)
- . 2024b, *MNRAS*, 528, 4314, doi: [10.1093/mnras/stae191](https://doi.org/10.1093/mnras/stae191)
- Dorn, C., Khan, A., Heng, K., et al. 2015, *A&A*, 577, A83, doi: [10.1051/0004-6361/201424915](https://doi.org/10.1051/0004-6361/201424915)
- Egger, J., Osborn, H., Kubyskhina, D., et al. 2024, *Astronomy & Astrophysics*, 688, A223
- Foley, B. J. 2024, *Reviews in Mineralogy and Geochemistry*, 90, 559, doi: [10.2138/rmg.2024.90.15](https://doi.org/10.2138/rmg.2024.90.15)
- Fortier, A., Simon, A., Broeg, C., et al. 2024, arXiv preprint arXiv:2406.01716
- Gaidos, E., Parviainen, H., Esparza-Borges, E., et al. 2024, *A&A*, 688, L34, doi: [10.1051/0004-6361/202451332](https://doi.org/10.1051/0004-6361/202451332)
- Grimm, S. L., Malik, M., Kitzmann, D., et al. 2021, *ApJS*, 253, 30, doi: [10.3847/1538-4365/abd773](https://doi.org/10.3847/1538-4365/abd773)
- Henning, T., Begemann, B., Mutschke, H., & Dorschner, J. 1995, *A&AS*, 112, 143
- Henning, T., & Mutschke, H. 1997, *A&A*, 327, 743
- Hon, M., Rappaport, S., Shporer, A., et al. 2025, arXiv e-prints, arXiv:2501.05431, doi: [10.48550/arXiv.2501.05431](https://doi.org/10.48550/arXiv.2501.05431)
- Hughes, A. M., Duchêne, G., & Matthews, B. C. 2018, *ARA&A*, 56, 541, doi: [10.1146/annurev-astro-081817-052035](https://doi.org/10.1146/annurev-astro-081817-052035)
- Jäger, C., Dorschner, J., Mutschke, H., Posch, T., & Henning, T. 2003, *A&A*, 408, 193, doi: [10.1051/0004-6361:20030916](https://doi.org/10.1051/0004-6361:20030916)
- Journaux, B., Kalousová, K., Sotin, C., et al. 2020, *SSRv*, 216, 7, doi: [10.1007/s11214-019-0633-7](https://doi.org/10.1007/s11214-019-0633-7)
- Jura, M., & Young, E. D. 2014, *Annual Review of Earth and Planetary Sciences*, 42, 45, doi: [10.1146/annurev-earth-060313-054740](https://doi.org/10.1146/annurev-earth-060313-054740)
- Kargel, J. S., & Lewis, J. S. 1993, *Icarus*, 105, 1, doi: [10.1006/icar.1993.1108](https://doi.org/10.1006/icar.1993.1108)
- Kawahara, H., Hirano, T., Kurosaki, K., Ito, Y., & Ikoma, M. 2013, *ApJL*, 776, L6, doi: [10.1088/2041-8205/776/1/L6](https://doi.org/10.1088/2041-8205/776/1/L6)
- Kite, E. S., Fegley, Bruce, J., Schaefer, L., & Gaidos, E. 2016, *ApJ*, 828, 80, doi: [10.3847/0004-637X/828/2/80](https://doi.org/10.3847/0004-637X/828/2/80)
- Kitzmann, D., & Heng, K. 2018, *MNRAS*, 475, 94, doi: [10.1093/mnras/stx3141](https://doi.org/10.1093/mnras/stx3141)
- Koike, C., Kaito, C., Yamamoto, T., et al. 1995, *Icarus*, 114, 203, doi: [10.1006/icar.1995.1055](https://doi.org/10.1006/icar.1995.1055)
- Kulterer, B. M., Wampfler, S. F., Ligterink, N. F. W., et al. 2024, *A&A*, 691, A281, doi: [10.1051/0004-6361/202450792](https://doi.org/10.1051/0004-6361/202450792)
- Laor, A., & Draine, B. T. 1993, *ApJ*, 402, 441, doi: [10.1086/172149](https://doi.org/10.1086/172149)
- Marsh, D., Solomon, S., & Reynolds, A. 2004, *Journal of Geophysical Research: Space Physics*, 109
- Matsuo, T., Greene, T. P., Johnson, R. R., et al. 2019, *PASP*, 131, 124502, doi: [10.1088/1538-3873/ab42f1](https://doi.org/10.1088/1538-3873/ab42f1)
- Meerdink, S. K., Hook, S. J., Roberts, D. A., & Abbott, E. A. 2019, *Remote Sensing of Environment*, 230, 111196, doi: [10.1016/j.rse.2019.05.015](https://doi.org/10.1016/j.rse.2019.05.015)
- Mie, G. 1908, *Annalen der Physik*, 330, 377, doi: [10.1002/andp.19083300302](https://doi.org/10.1002/andp.19083300302)
- Miguel, Y., Kaltenecker, L., Fegley, B., & Schaefer, L. 2011, *ApJL*, 742, L19, doi: [10.1088/2041-8205/742/2/L19](https://doi.org/10.1088/2041-8205/742/2/L19)
- O'Neill, H. S. C., & Palme, H. 1998, *Composition of the Silicate Earth: Implications for Accretion and Core Formation* (Cambridge University Press), 3 – 126, doi: [10.1017/CBO9780511573101.004](https://doi.org/10.1017/CBO9780511573101.004)
- Palik, E. D. 1985, *Handbook of optical constants of solids*
- . 1991, *Handbook of optical constants of solids II*
- Perez-Becker, D. A. 2013, PhD thesis, University of California, Berkeley
- Pollack, J. B., Hollenbach, D., Beckwith, S., et al. 1994, *ApJ*, 421, 615, doi: [10.1086/173677](https://doi.org/10.1086/173677)
- Posch, T., Kerschbaum, F., Fabian, D., et al. 2003, *ApJS*, 149, 437, doi: [10.1086/379167](https://doi.org/10.1086/379167)
- Rappaport, S., Levine, A., Chiang, E., et al. 2012, *The Astrophysical Journal*, 752, 1, doi: [10.1088/0004-637x/752/1/1](https://doi.org/10.1088/0004-637x/752/1/1)
- Sanchis-Ojeda, R., Rappaport, S., Pallè, E., et al. 2015, *The Astrophysical Journal*, 812, 112
- Scarpa, R., Tilling, R. I., & Giggenbach, W. 1996, *Monitoring and mitigation of volcano hazards*, 221
- Schaefer, L., & Fegley, B. 2009, *ApJL*, 703, L113, doi: [10.1088/0004-637X/703/2/L113](https://doi.org/10.1088/0004-637X/703/2/L113)
- Schlawin, E., Herter, T., Zhao, M., Teske, J. K., & Chen, H. 2016, *ApJ*, 826, 156, doi: [10.3847/0004-637X/826/2/156](https://doi.org/10.3847/0004-637X/826/2/156)
- Schlawin, E., Hirano, T., Kawahara, H., et al. 2018, *AJ*, 156, 281, doi: [10.3847/1538-3881/aaeb32](https://doi.org/10.3847/1538-3881/aaeb32)
- Schlawin, E., Su, K. Y. L., Herter, T., Ridden-Harper, A., & Apai, D. 2021, *AJ*, 162, 57, doi: [10.3847/1538-3881/ac0b41](https://doi.org/10.3847/1538-3881/ac0b41)
- Schlawin, E., Mukherjee, S., Ohno, K., et al. 2024a, *AJ*, 168, 104, doi: [10.3847/1538-3881/ad58e0](https://doi.org/10.3847/1538-3881/ad58e0)
- Schlawin, E., Ohno, K., Bell, T. J., et al. 2024b, *ApJL*, 974, L33, doi: [10.3847/2041-8213/ad7fef](https://doi.org/10.3847/2041-8213/ad7fef)
- Seager, S., Kuchner, M., Hier-Majumder, C. A., & Militzer, B. 2007, *ApJ*, 669, 1279, doi: [10.1086/521346](https://doi.org/10.1086/521346)
- Sinnhuber, M., Nieder, H., & Wieters, N. 2012, *Surveys in Geophysics*, 33, 1281
- Swain, M. R., Hasegawa, Y., Thorngren, D. P., & Roudier, G. M. 2024, *SSRv*, 220, 61, doi: [10.1007/s11214-024-01098-7](https://doi.org/10.1007/s11214-024-01098-7)
- Thiabaud, A., Marboeuf, U., Alibert, Y., Leya, I., & Mezger, K. 2015, *A&A*, 580, A30, doi: [10.1051/0004-6361/201525963](https://doi.org/10.1051/0004-6361/201525963)

- Ueda, K., Yanagi, H., Noshiro, R., Hosono, H., & Kawazoe, H. 1998, *Journal of Physics Condensed Matter*, 10, 3669, doi: [10.1088/0953-8984/10/16/018](https://doi.org/10.1088/0953-8984/10/16/018)
- van Lieshout, R., Min, M., & Dominik, C. 2014, *A&A*, 572, A76, doi: [10.1051/0004-6361/201424876](https://doi.org/10.1051/0004-6361/201424876)
- van Lieshout, R., Min, M., Dominik, C., et al. 2016, *A&A*, 596, A32, doi: [10.1051/0004-6361/201629250](https://doi.org/10.1051/0004-6361/201629250)
- Vanderburg, A., Johnson, J. A., Rappaport, S., et al. 2015, *Nature*, 526, 546, doi: [10.1038/nature15527](https://doi.org/10.1038/nature15527)
- Wang, H. S., Liu, F., Ireland, T. R., et al. 2019, *MNRAS*, 482, 2222, doi: [10.1093/mnras/sty2749](https://doi.org/10.1093/mnras/sty2749)
- Welbanks, L., Bell, T. J., Beatty, T. G., et al. 2024, *Nature*, 630, 836, doi: [10.1038/s41586-024-07514-w](https://doi.org/10.1038/s41586-024-07514-w)
- Zeidler, S., Posch, T., Mutschke, H., Richter, H., & Wehrhan, O. 2011, *A&A*, 526, A68, doi: [10.1051/0004-6361/201015219](https://doi.org/10.1051/0004-6361/201015219)

## APPENDIX

## A. OUTLIER REMOVAL

Figure A1 shows the stellar spectrum from MIRI, time averaged over the fourth observation. The turnover below  $5 \mu\text{m}$  is due to reduced throughput in slitless mode. The red “x” points indicate outliers in the spectrum that deviated from neighboring points in a 9-channel wide sliding window by  $3\sigma$ . These outliers were removed from the data as a first step before subsequent analysis.

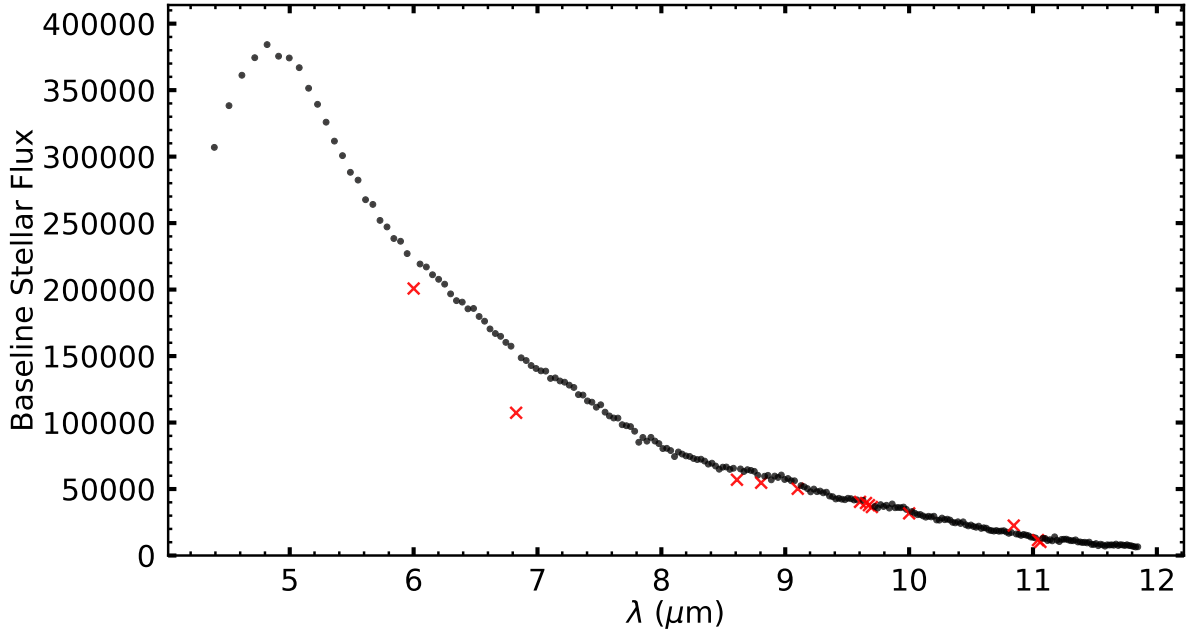


**Figure A1.** Time-averaged stellar spectrum with flux outliers removed. Turnover below  $5 \mu\text{m}$  is due to reduced throughput. A sliding window of 9 channels was used to identify points with a greater than  $3\sigma$  deviation from its neighbors. Red “x” points are the outliers that were removed.

## B. LIGHTCURVES

Figure B2 shows the cleaned time series data for all four transit observations described in §2 and listed in Table 1. The first 30 minutes of data was removed from each observation to account for settling. The baseline of each observation was conservatively estimated as the flux outside  $1.5\times$  the 46 average transit duration determined by Sanchis-Ojeda et al. (2015). For observations 1, 2 and 3, a line was fit to the baseline flux and divided out to detrend any residual ramp remaining after the Eureka! pipeline reduction. The reported uncertainties from Eureka! were inflated to match the standard deviation in the baseline flux.

Multiple bin sizes were tried, and we ultimately settled on binning to a time resolution of 8 minutes ( $N=21$ ). Figure B3 shows the results from the allan variance plot, supporting the optimal bin choice. We constructed a lightcurve model by fitting a 2-degree polynomial to these binned up points in the transit window of transit 4, and setting the model to the mean of the baseline flux elsewhere. This model was then applied to each transit observation, centered around the ephemeris and scaled to measure the transit depth. These measurements are listed in Table 1. The residuals for these models is shown in the bottom panels of each lightcurve in Figure B2. Other lightcurve models were also tested, including the average  $K2$  lightcurve, and a simple boxcar. The resulting spectra from fitting these models to the spectroscopic channels showed no significant difference, indicating our results are not sensitive to our choice of lightcurve model.

The same lightcurve models were tested on the CHEOPS photometry, also showing no significant difference in the results. Figure B4 shows the fit of our chosen 2-degree polynomial model to the detrended CHEOPS data over the

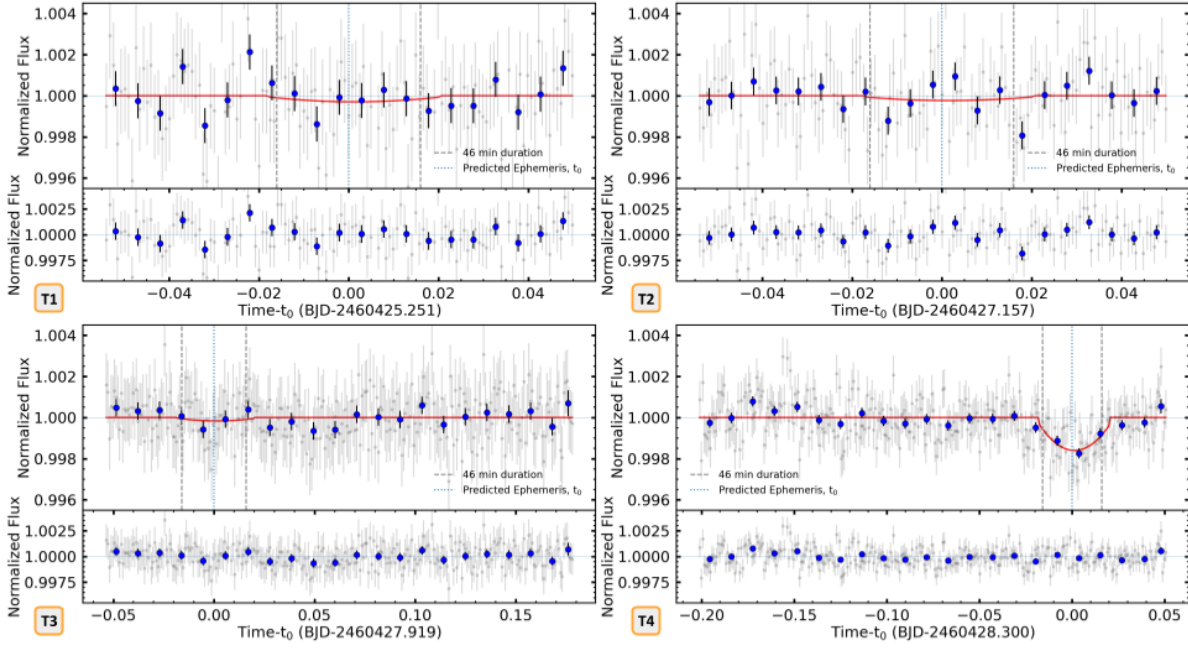


**Figure B2.** MIRI LRS lightcurves for all 4 transit observations listed in Table 1. The unbinned data are greyed out in the background. The blue points are binned to a time resolution of 8 minutes. The red line is a 2nd order polynomial fit to transit 4 and scaled to the best fit value in each window. Multiple transit models were fit, including the original *K2* lightcurve and a boxcar, with no significant difference. The 46 min transit duration calculated by Sanchis-Ojeda et al. (2015) is included as vertical gray dashed lines for reference. The uncertainties in the data points as reported by *Eureka!* were inflated to match the actual standard deviation in the baseline flux.

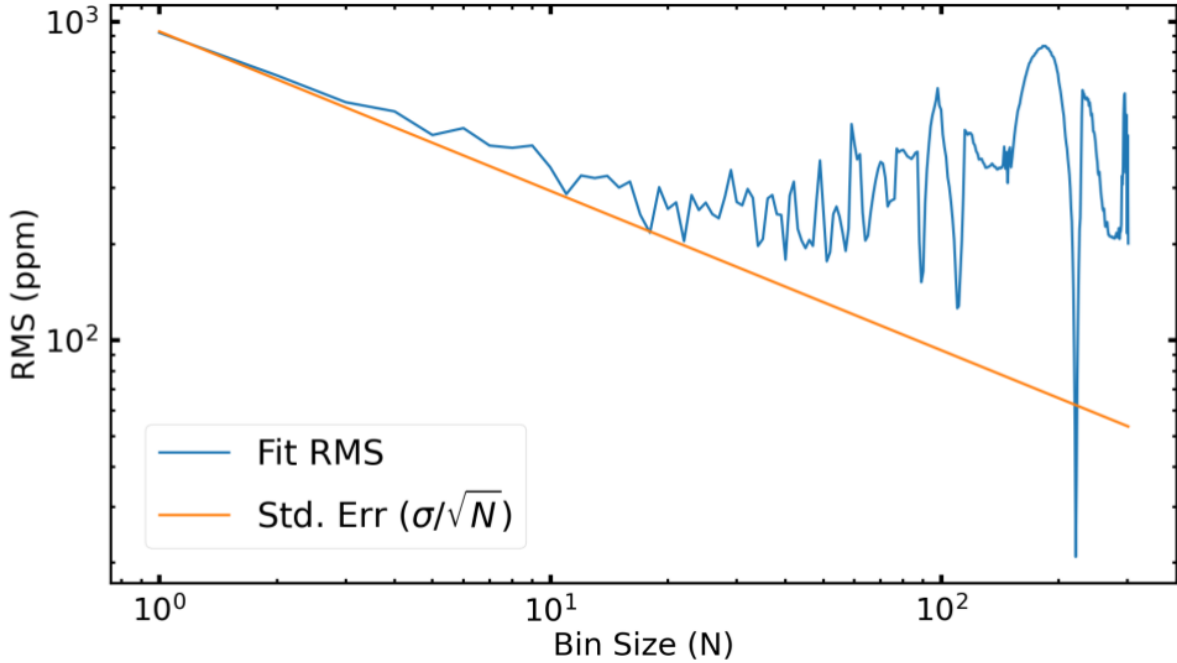


**Figure B3.** Allan variance plot for the lightcurve of transit 4. The blue line shows the RMS of the model fit to the data for different bin sizes. The orange line shows the median of the uncertainties in each data point as they are binned up. The uncertainties in the data points as reported by *Eureka!* were inflated to match the actual standard deviation in the baseline flux.

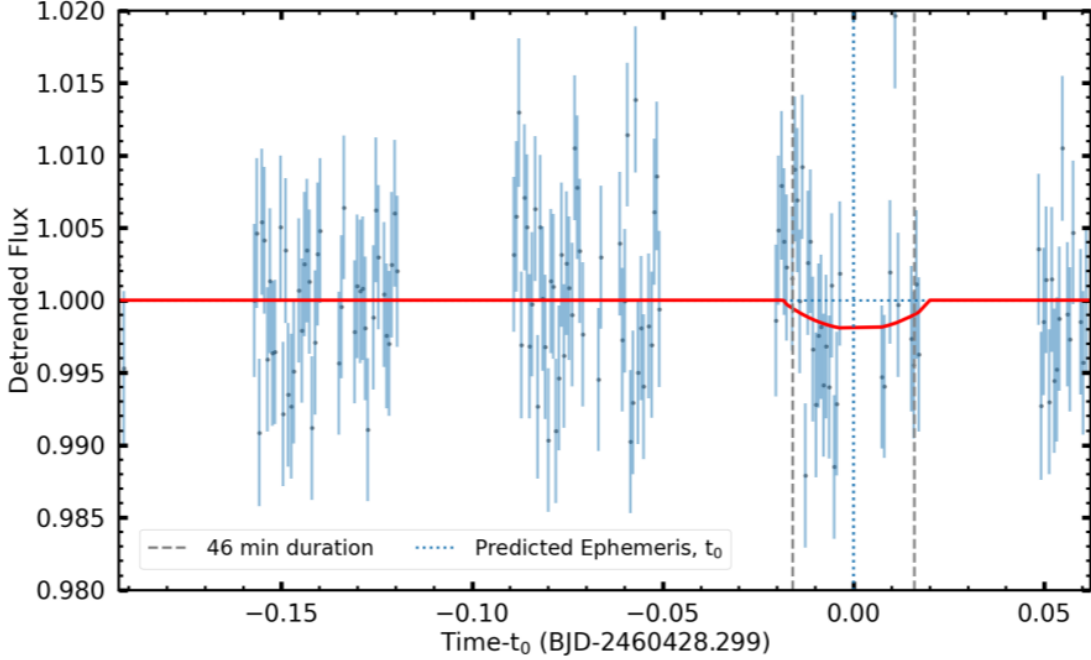


**Figure B4.** Detrended CHEOPS photometry during transit 4. The red line is a 2nd order polynomial fit to the transit window and zero elsewhere. Multiple transit models were fit, including the original *K2* lightcurve and a boxcar, with no significant difference. The 46min transit duration calculated by [Sanchis-Ojeda et al. \(2015\)](#) is included for reference. Gaps in the data were caused by occultations of Earth during the space telescope’s orbit. The other three transit windows fall in these gaps.

transit window. We measured the depth and associated uncertainty of each transit fit using equations 1 & 2. Given the CHEOPS bandpass of 330–1100 nm, we added this photometric point to our JWST spectrum as an optical depth constraint.

### C. SPECTRA VALIDATION

Although the white-light time series for transits 1, 2, and 3 show no transit, we produced a spectrum for each transit window by fitting our transit model to each spectral channel. The top panel of Figure C5 shows the resulting fit for each observation. The data is binned the same for each observation ( $R=17$ ) and shows significant depth in the 4.5 and 5.1  $\mu\text{m}$  channels in the transits 1, 2, 3, despite their low overall white-light transit depth. And in every observation, the spectra show transparency in the 4.8  $\mu\text{m}$  bin.

The bottom panel of Figure C5 shows a stacked spectrum of all four transits. To stack these spectra we first added the time series flux in each channel centered around the ephemeris for each observation. We then fit our transit model to the combined time series flux in each channel and binned as before ( $R=17$ ) to produce the combined spectrum. The most significant features are still present at 4.5 and 5.1  $\mu\text{m}$  even with reduced overall white-light transit depth.

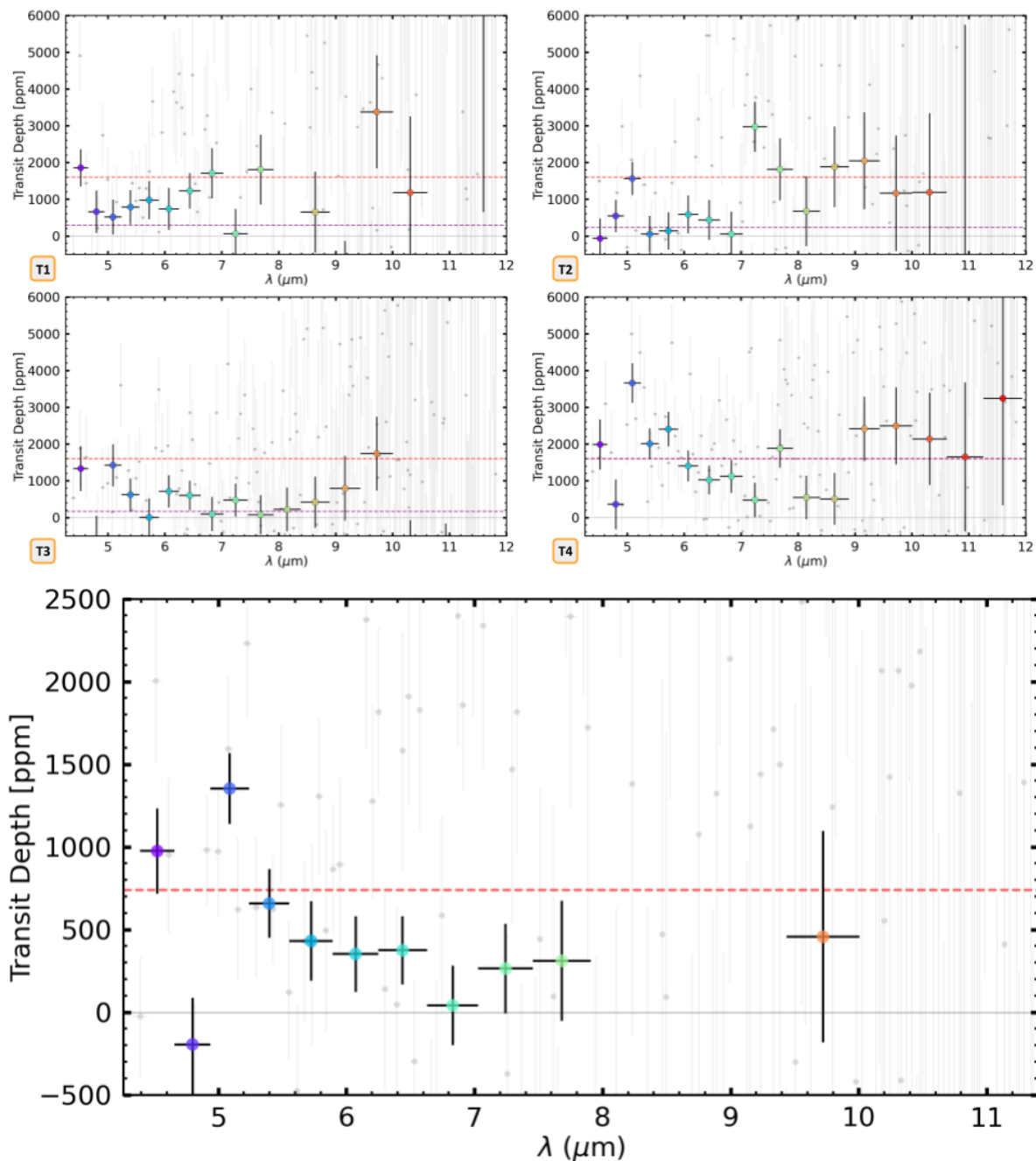


**Figure C5.** MIRI spectra during all four expected transits using the 2-degree transit model from transit 4, scaled to the optimal depth in each channel for each transit.

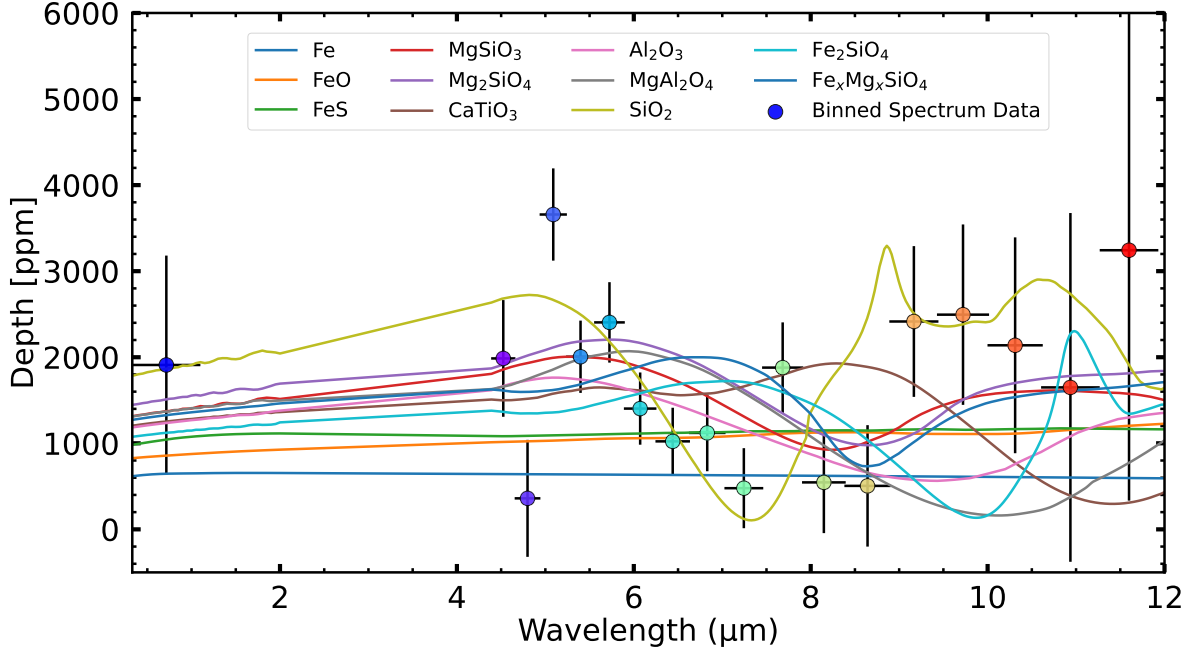
*Top:* Individual spectra during each transit window. The red dashed line marks the overall transit depth in T4. The purple dashed line indicates the overall transit depth in each observation as measured from the white-light lightcurves. The white-light time series of transit 4 shows a clear signal, while the others do not (see Figure B2). However, the most or second most significant detections in T1, T2 and T3 are in the 4.5 and 5.1  $\mu\text{m}$  channels, supporting the reality of these narrow features observed at modest significance in T4.

*Bottom:* Combined spectra of all four transits. The 4.5 and 5.1  $\mu\text{m}$  features are clearly evident.

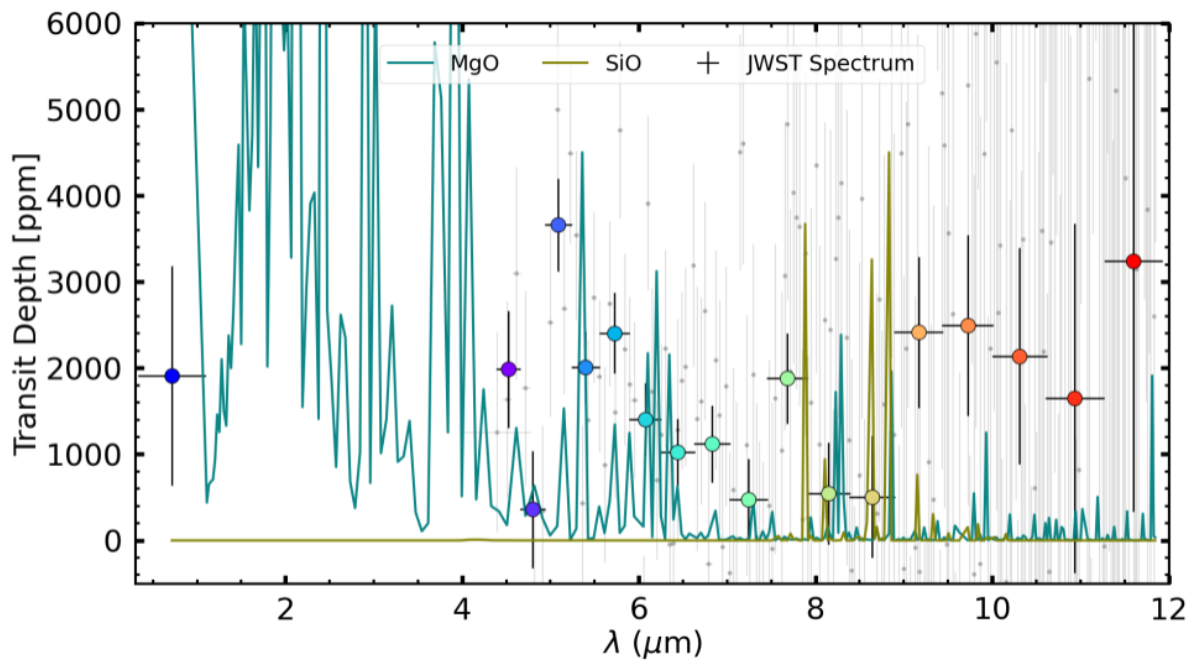
## D. SOLID AND GAS OPACITIES

Figure D6 shows the solid mineral opacities constructed from Mie scattering theory using the optical properties in Table E1. We assumed a power law ( $p = 0.875$ ) distribution of  $0.01\text{--}5\ \mu\text{m}$  grains for an effective grain size of  $1\ \mu\text{m}$ . Representative species for core, mantle and crust mineralogy were tested, see §3.1. The spectrum is inconsistent with featureless iron dust from a bare core. No combination of solid mineralogy is able to fit all of the spectral features. In particular, the distinct features from  $4.3\text{--}6\ \mu\text{m}$  are not accounted for in any of the solid mineralogy we tested.

These dramatic features from  $4.3\text{--}6\ \mu\text{m}$  seem indicative of molecular gas features. We tested many plausible gas species from the DACE database at high temperature ( $2100\ \text{K}$ ) and low pressure ( $10^{-8}\ \text{bar}$ ) against the data. See §3.2. Figure D7 shows the two most theoretically plausible gases from vaporizing Earth-like mantle material. The poor fit to the data suggests these gases are not detected. Figure D8 shows two gases that fit the  $4.3\text{--}6\ \mu\text{m}$  features in the data much better.



**Figure D6.** Opacities calculated from optical properties of solid dust species using Mie scattering theory with an effective dust grain size of  $1\ \mu\text{m}$  for a power law ( $p = 0.875$ ) distribution of dust grains. Representative models for core, mantle and crust mineralogy are included. This spectrum disfavors purely featureless iron compounds indicative of a bare core. None of these solid dust opacities simultaneously account for all the features in the spectrum, particularly falling short of describing the feature around  $5\ \mu\text{m}$ .



**Figure D7.** Gas opacities of rock vapor from the DACE database overlaid with the MIRI data. The two most theoretically plausible species expected from typical mantle material are shown: MgO and SiO (Booth et al. 2023). These poorly fit the data indicating these gases are not detected in the MIRI data.

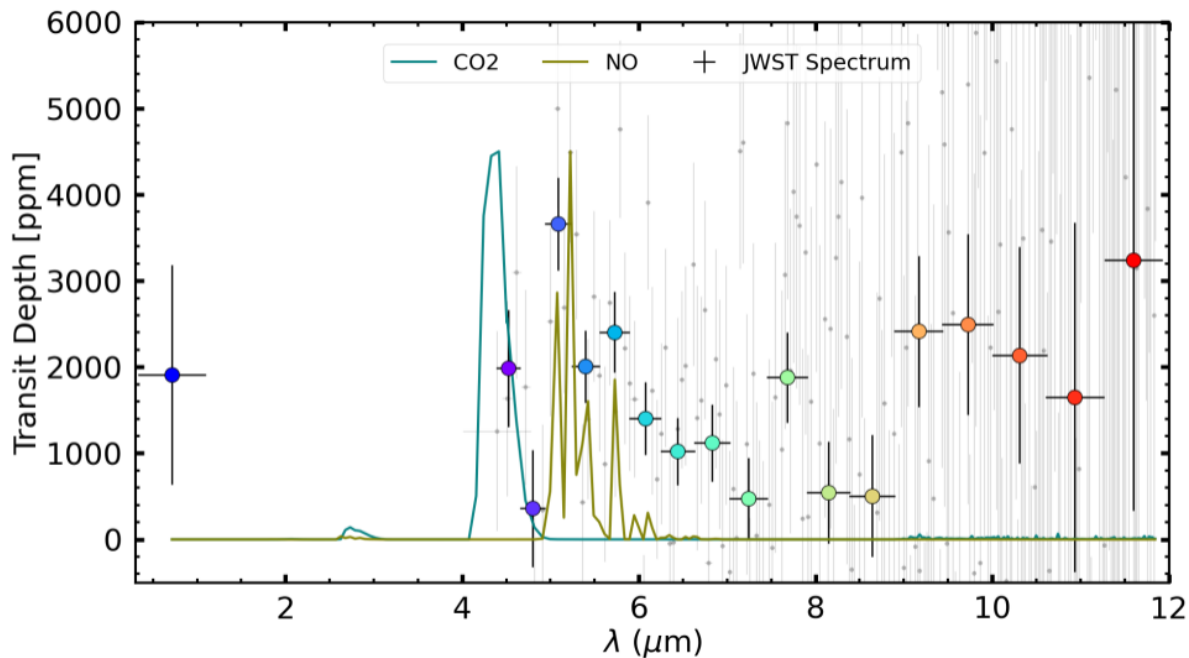


**Figure D8.** Gas opacities of ices overlaid with the MIRI data. Many different ice species were considered from the DACE database. The best fitting gas models are nitric oxide, NO, and carbon dioxide, CO<sub>2</sub> to explain the short-wavelength features from 4.3~6 μm.



## E. OPTICAL DATA REFERENCES

**Table E1.** Dust optical data sources. For details on the wavelength ranges please refer to Table 1 in [Kitzmann & Heng \(2018\)](#).

Condensate	Reference
Al <sub>2</sub> O <sub>3</sub> [s]	<a href="#">Begemann et al. (1997)<sup>*t</sup></a> ; <a href="#">Koike et al. (1995)<sup>t</sup></a>
CaTiO <sub>3</sub> [s]	<a href="#">Posch et al. (2003)<sup>t</sup></a> ; <a href="#">Ueda et al. (1998)<sup>f</sup></a>
Fe [s]	Lynch & Hunter in <a href="#">Palik (1991)<sup>t</sup></a>
Fe <sub>0.4</sub> Mg <sub>0.6</sub> O [s]	<a href="#">Henning et al. (1995)<sup>*t</sup></a>
Fe <sub>0.7</sub> Mg <sub>0.3</sub> O [s]	<a href="#">Henning et al. (1995)<sup>*t</sup></a>
Fe <sub>2</sub> SiO <sub>4</sub> [s]	unpublished*
FeO [s]	<a href="#">Henning et al. (1995)<sup>*t</sup></a>
FeS [s]	<a href="#">Pollack et al. (1994)<sup>t</sup></a> ; <a href="#">Henning &amp; Mutschke (1997)<sup>t</sup></a>
Mg <sub>2</sub> SiO <sub>4</sub> [s]	<a href="#">Jäger et al. (2003)<sup>*t</sup></a>
MgSiO <sub>3</sub> [s]	<a href="#">Jäger et al. (2003)<sup>*t</sup></a>
MgAl <sub>2</sub> O <sub>4</sub> [s]	<a href="#">Zeidler et al. (2011)</a> ; <a href="#">Tropf &amp; Thomas in Palik (1991)<sup>t</sup></a>
SiC [s]	<a href="#">Laor &amp; Draine (1993)<sup>t</sup></a>
SiO <sub>2</sub> [s]	<a href="#">Henning &amp; Mutschke (1997)<sup>*t</sup></a> ; <a href="#">Philipp in Palik (1985)<sup>t</sup></a>

We note we use the amorphous (sol-gel) data for Mg<sub>2</sub>SiO<sub>4</sub>[s] and MgSiO<sub>3</sub>[s], and the amorphous data for SiO<sub>2</sub>[s].

\*Data from the Database of Optical Constants for Cosmic Dust, Laboratory Astrophysics Group of the AIU Jena.

<sup>t</sup>Data from a printed or digital table.

<sup>f</sup>Data from a figure.